

Article

Pyroxenite as a Product of Mafic-Carbonate Melt Interaction (Tazheran Massif, West Baikal Area, Russia)

Eugene V. Sklyarov ^{1,2,*} , Andrey V. Lavrenchuk ^{2,3}, Anna G. Doroshkevich ^{2,4}, Anastasia E. Starikova ^{2,3} and Sergei V. Kanakin ⁴

¹ Institute of the Earth's Crust, Siberian Branch of the Russian Academy of Sciences, 664033 Irkutsk, Russia

² V.S. Sobolev Institute of Geology and Mineralogy, Siberian Branch of the Russian Academy of Sciences, 630090 Novosibirsk, Russia; alavr@uiggm.nsc.ru (A.V.L.); doroshkevich@igm.nsc.ru (A.G.D.); starikova@igm.nsc.ru (A.E.S.)

³ Department of Geology and Geophysics, Novosibirsk State University, 630090 Novosibirsk, Russia

⁴ Geological Institute, Siberian Branch of the Russian Academy of Sciences, 670047 Ulan-Ude, Russia; skan_61@mail.ru

* Correspondence: skl@crust.irk.ru; Tel.: +7-914-908-9408

Abstract: Pyroxenite and nepheline-pyroxene rocks coexist with dolomite-bearing calcite marbles in Tazheran Massif in the area of Lake Baikal, Siberia, Russia. Pyroxenites occur in a continuous elongate zone between marbles and beerbachites (metamorphosed gabbro dolerites) and in 5 cm to 20 m fragments among the marbles. Pyroxene in pyroxenite is rich in calcium and alumina (5–12 wt% Al₂O₃) and has a fassaite composition. The Tazheran pyroxenite may originate from a mafic subvolcanic source indicated by the presence of remnant dolerite found in one pyroxenite body. This origin can be explained in terms of interaction between mafic and crust-derived carbonatitic melts, judging by the mineralogy of pyroxenite bodies and their geological relations with marbles. According to this model, the intrusion of mantle mafic melts into thick lower crust saturated with fluids caused partial melting of silicate-carbonate material and produced carbonate and carbonate-silicate melts. The fassaite-bearing pyroxenite crystallized from a silicate-carbonate melt mixture which was produced by roughly synchronous injections of mafic, pyroxenitic, and carbonate melt batches. The ascending hydrous carbonate melts entrained fragments of pyroxenite that crystallized previously at a temperature exceeding the crystallization point of carbonates. Subsequently, while the whole magmatic system was cooling down, pyroxenite became metasomatized by circulating fluids, which led to the formation of assemblages with garnet, melilite, and scapolite.



Citation: Sklyarov, E.V.; Lavrenchuk, A.V.; Doroshkevich, A.G.; Starikova, A.E.; Kanakin, S.V. Pyroxenite as a Product of Mafic-Carbonate Melt Interaction (Tazheran Massif, West Baikal Area, Russia). *Minerals* **2021**, *11*, 654. <https://doi.org/10.3390/min11060654>

Academic Editor: Federica Zaccarini

Received: 10 May 2021

Accepted: 18 June 2021

Published: 20 June 2021

Publisher's Note: MDPI stays neutral with regard to jurisdictional claims in published maps and institutional affiliations.



Copyright: © 2021 by the authors. Licensee MDPI, Basel, Switzerland. This article is an open access article distributed under the terms and conditions of the Creative Commons Attribution (CC BY) license (<https://creativecommons.org/licenses/by/4.0/>).

Keywords: pyroxenite; marble; gabbro dolerite; mafic melt; carbonate melt; silicate-carbonate melt interaction; fluids; metasomatism; Early Paleozoic orogeny; Tazheran Massif

1. Introduction

Interaction of silicate and carbonate magmas is a common process responsible for the compositional diversity of the crust. Intruding melts and related fluids either cause isochemical thermal and metasomatic alteration to carbonate country rocks, with skarn and other metasomatic effects ([1–3] and references therein), or become assimilated by silicate magma, thus changing its composition [4–8], etc. These processes produce unusual mineral assemblages, which often include Ca-Al-rich pyroxene almost free from alkalis, called fassaite. Note that the latest classification of pyroxenes by Morimoto et al. [9] does not list fassaite as a separate mineral species but rather names it *ferrian aluminian diopside* or *augite*. In our view though, fassaite is a more appropriate term than these [9], because the former is too long while the latter is simply wrong: the Ca contents in the mineral exceed that defined for augite ($X_{Ca} \sim 0.50$ against 0.45, respectively).

Fassaite sometimes occurs in xenoliths of metasomatized carbonates among mafic or alkaline mafic rocks [6,10–12], etc.) but is most often found in metamorphic limestone near

intrusive contacts [10] and references therein. Occasionally, it appears as phenocrysts in alkaline ultramafics and in Ca-Al-rich inclusions in meteorites, as in the case of Allende [10]. Fassaite can sometimes crystallize directly from mafic melts contaminated with carbonates, but most often it forms by a strong thermal effect on carbonates, which are either located near the intrusive contacts or occur in xenoliths entrained with magma. However, monomineral fassaite and nepheline-fassaite rocks from the Tazheran Massif in the western side of Lake Baikal (Siberia, Russia) exist as independent bodies related neither to intrusive contacts nor to xenoliths. This is a synthesis of data on the geological setting, major- and trace-element chemistry, and mineralogy of the Tazheran fassaitic rocks, with implications for their unusual origin otherwise than in classical metasomatic reactions.

2. Geological Background

Tazheran Massif is a syenite and nepheline syenite complex located within the Olkhon metamorphic terrane (Figure 1), which is part of the Early Paleozoic Baikal collisional system [13–15] in the southern periphery of the Siberian craton [16]. The Olkhon terrane is a collage of compositionally and genetically diverse shear zones consisting of gneiss, amphibolite, calcite, and dolomite marbles, and quartzites derived from different protoliths [16,17] and references therein, as well as diverse igneous lithologies, such as granite, syenite (including nepheline-bearing varieties), gabbro, and ultramafics. The terrane comprises amphibolite-carbonate (1), rather gneissic (2), and marble-gneissic-mafic (3) tectonic units (Figure 2). The igneous rocks in the three units are large gabbro intrusions in unit 1; granitoid, gabbro, and ultramafic intrusions coexisting with less abundant amphibolite and marble in unit 2, and small gabbro and granite bodies in unit 3. The tectonic framework of the terrane results from its collision with the craton and the related strike-slip faulting at Early Paleozoic orogeny [18–20].

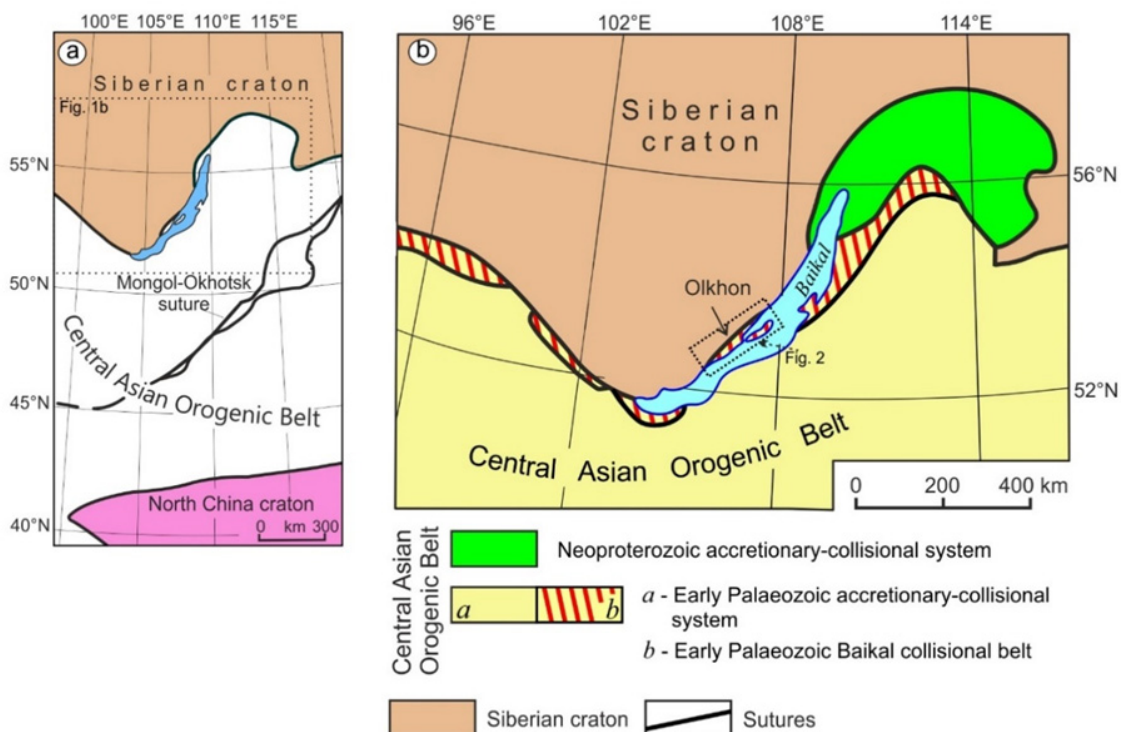


Figure 1. Simplified tectonics of Central Asia (a) and terranes in the Early Paleozoic Baikal collisional belt of northern CAOB (b), modified after [17].

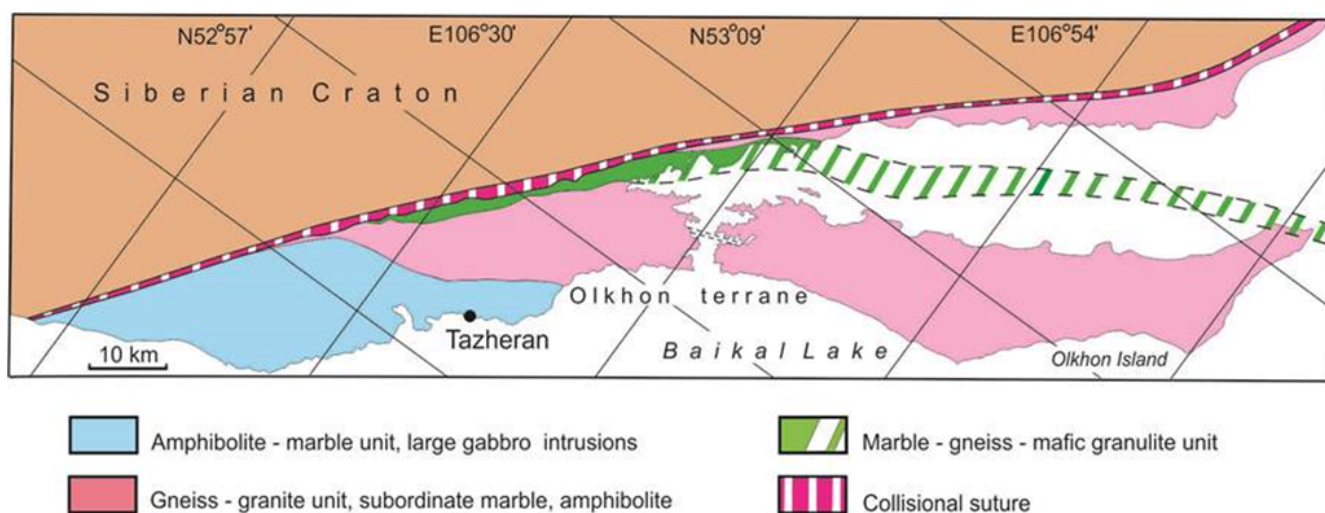


Figure 2. Simplified tectonics of the Olkhon terrane, modified after [15]. Tazheran Massif is shown as a black circle.

The Tazheran complex of intricately interfingering igneous, metamorphic, and metasomatic rocks (Figure 3) is unique in many respects, including the metasomatic diversity [13] and relations between intrusions and carbonate country rocks [15,21]. The igneous lithologies are mainly gabbro-dolerite and gneissic syenite, less abundant subalkaline gabbro, and rare nepheline syenite. Almost all gabbro-dolerite, except for a few remnant fragments, has been converted to beerbachite, which is fine-grained massive or gneissic rock with a mineralogy of Cpx + Opx + Pl + Ilm + Bt + Ol + Amp + Spl + Ti-Mag (Here and below mineral abbreviations are after [22]). Nepheline syenite occurs as linear or more intricately shaped veins from 20 cm to, more rarely, a few meters thick. The rocks have some age constraints: 470 Ma for syenite, approximately the same U-Pb baddeleyite age for remnant dolerite in beerbachite, and the 451–464 Ma range for Ne-syenite [15]. The age of strongly metamorphosed gneissic subalkaline gabbro may be extrapolated from the 461 Ma date of compositionally identical rocks found elsewhere in the Olkhon terrane [23].

The abundant metasomatic rocks are of magnesian, alkaline, or calcic affinities [24]. Magnesian metasomatites common to the southern part of the complex are either skarn and calc-silicate rocks at the contact between Ne-syenite and brucite marble or veins in the latter, which are more often found near (but not immediately at) or away from the Ne-syenite contact [25]. Alkaline metasomatites coexisting with dolomite-bearing calcite marbles in the middle of the complex (Figure 3) are Ti fassaite-nepheline rocks and related metasomatic garnet-melilite-diopside-wollastonite varieties with minor percentages of nepheline or kalsilite (see below). Calcic metasomatites appear in a band of calcite marbles on the periphery of the complex together with linear amphibolite bodies (altered mafic dikes). Some metasomatites are typical medium-temperature garnet-pyroxene (\pm Amp, \pm Ep, \pm An) skarns that form thin (≤ 10 cm) zones at the amphibolite-marble contacts or inside amphibolite, or sometimes occur as up to 20 m bodies with remnant amphibolite.

Pyroxenite and nepheline-fassaite rocks make up a W–E zone, about 600 m long and up to 160–170 m wide, in the interior of the complex (Figure 4), where they coexist with coarse- to giant-grained (0.5 to 40 mm) dolomite-bearing calcite marbles (Marble is here a non-genetic description for carbonate rocks). In the northern part of the complex, marbles enclose more or less strongly skarned pyroxenite boudins which vary in size from 0.2 to 15–20 m (Figure 5A–C) but most often are 1 cm to 15 cm angular fragments (Figure 5D,E), sometimes resorbed (Figure 5F). The pyroxenite zone borders beerbachites in the north, syenites in the south, and Cpx-Wo-Pl and Grt-Me-Wo-Cpx metasomatites in the west. The syenites, which are mostly buried in the west (except for a few outcrops used for reference in mapping the contact line), and the better exposed beerbachites have sharp contacts free from signatures of metasomatism.

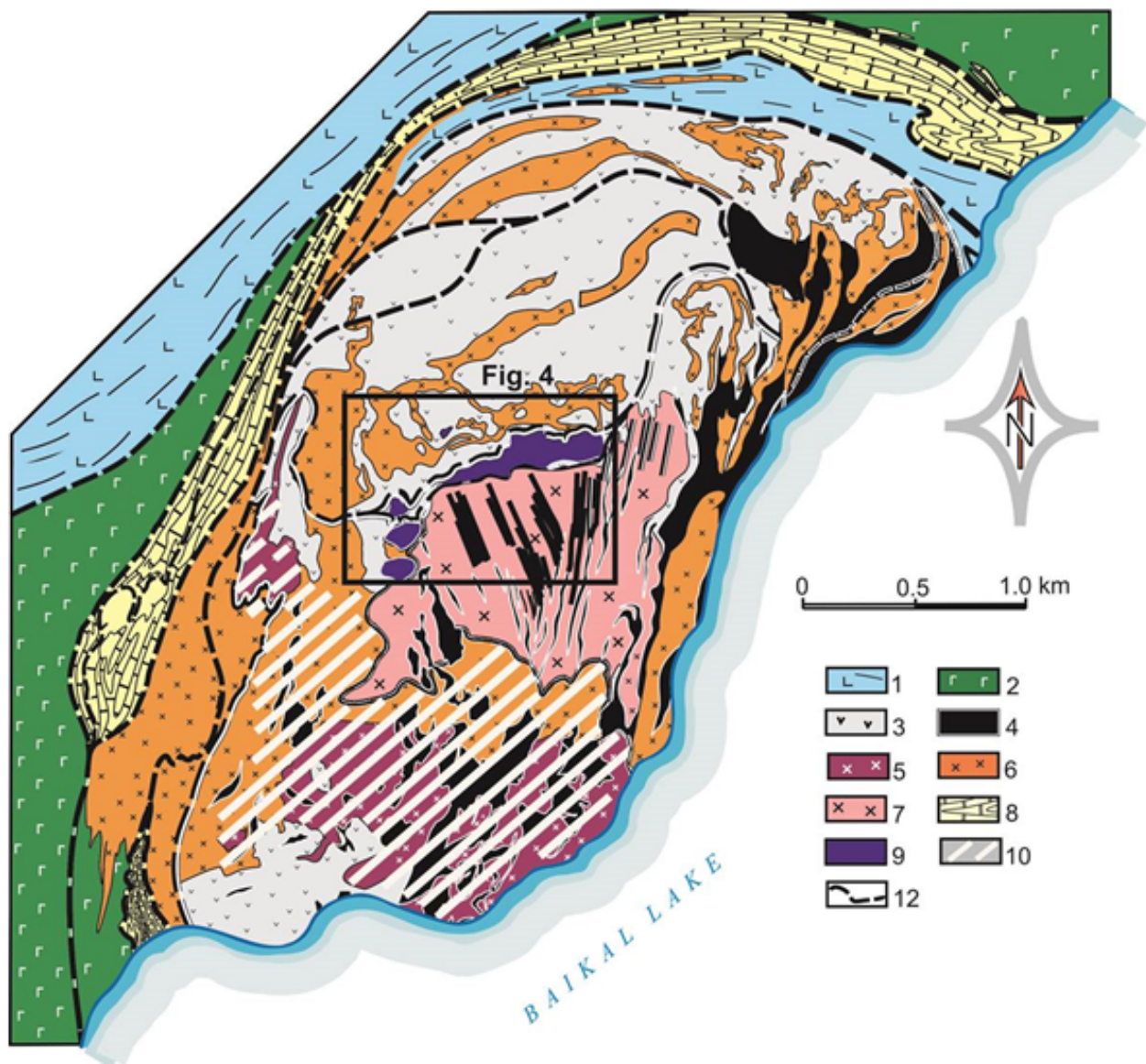


Figure 3. Simplified geology of Tazheran Massif, modified after [14,23]: 1–2 = country rocks, 500 Ma: amphibolite, silicate-carbonate gneiss (1); metamorphosed gabbro, monzogabbro, monzonite, and syenite (2); 3–7 = Tazheran Massif, 460–470 Ma: beerbachite after tholeiitic dolerite and gabbro (3), subalkaline gabbro and microgabbro (4), nepheline syenite (5), foliated (6) and massive (7) syenites; 8–10 = calcic (8), alkaline (9), and magnesian (10) metasomatic rocks; 11 = synmetamorphic ductile detachment; 12 = geological boundaries. You can view “Image” in Figure 4.

Pyroxenite is a black fine-grained rock with variable percentages of nepheline: within 10% in pyroxenite proper and 30% to 50 % in nepheline-pyroxene rocks. The latter occur as randomly distributed irregularly shaped meters-long lenses in pyroxenite, with smooth boundaries. The mineralogy of pyroxenite and nepheline-pyroxene rocks consists of nepheline, amphibole, spinel, and rare calcite, perovskite, and biotite. Some pyroxenite samples contain rare disseminated Co-Ni-bearing loellingite or nickeline and westerveldite. Small pyroxenite clasts in marbles and the margins of large bodies are often metasomatized and bear grossular-andradite garnets or rarely melilite and monticellite; garnet-scapolite-pyroxene skarn is sometimes superposed over that of nepheline-garnet-fassaite.

One elongate drop-shaped pyroxenite body (Figure 6), about 20 m long and up to 8 m wide, encloses a small boudin of dense dark gray remnant ophitic dolerite (Figure 7A,B) with skarned margins, in which recrystallized melanocratic minerals (Ol, Cpx, Pg, and Bt) are set in a matrix of plagioclase laths or appear as phenocrysts.

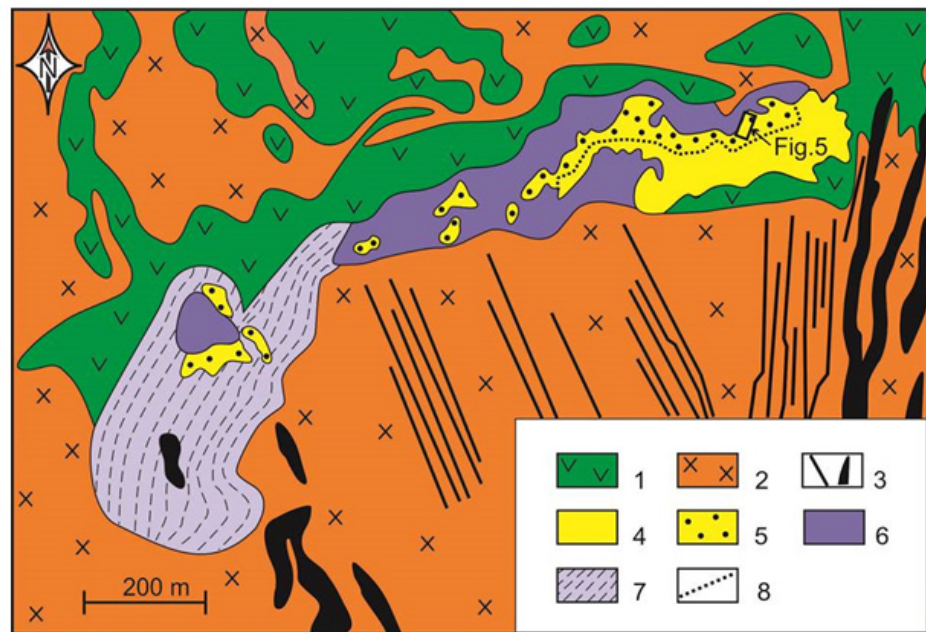


Figure 4. Simplified local geology of pyroxenite and nepheline-fassaite rocks and their surroundings. 1 = beerbachite after tholeiitic dolerite and gabbro; 2 = syenite; 3 = subalkaline gabbro and microgabbro; 4,5 = dolomite-bearing calcite marble (4) with abundant pyroxenite fragments (5); 6 = pyroxenite and nepheline-fassaite rocks; 7 = garnet-melilite-pyroxene and melilite-wollastonite metasomatic rocks; 8 = boundary between pyroxenite-bearing and pyroxenite-free marbles.



Figure 5. Pyroxenite in marbles. (A) a large pyroxenite fragment (up to 15 m in diameter); (B) a lens of skarned pyroxenite; (C) a few pyroxenite fragments; (D,E) small fragments of skarned pyroxenite; (F) a fragment of skarned pyroxenite “dissolved” along the margins.

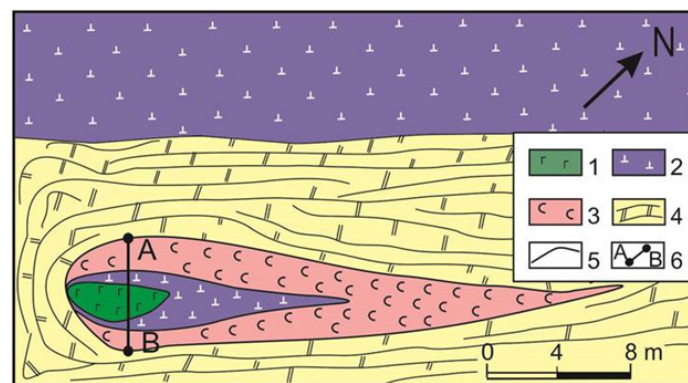


Figure 6. Geological sketch of a pyroxenite fragment with remnant dolerite in the middle. 1 = dolerite; 2 = pyroxenite; 3 = skarned pyroxenite; 4 = marble; 5 = geological boundaries; 6 = sampled profile from SE1250c1 (A) to SE1250c20 (B).

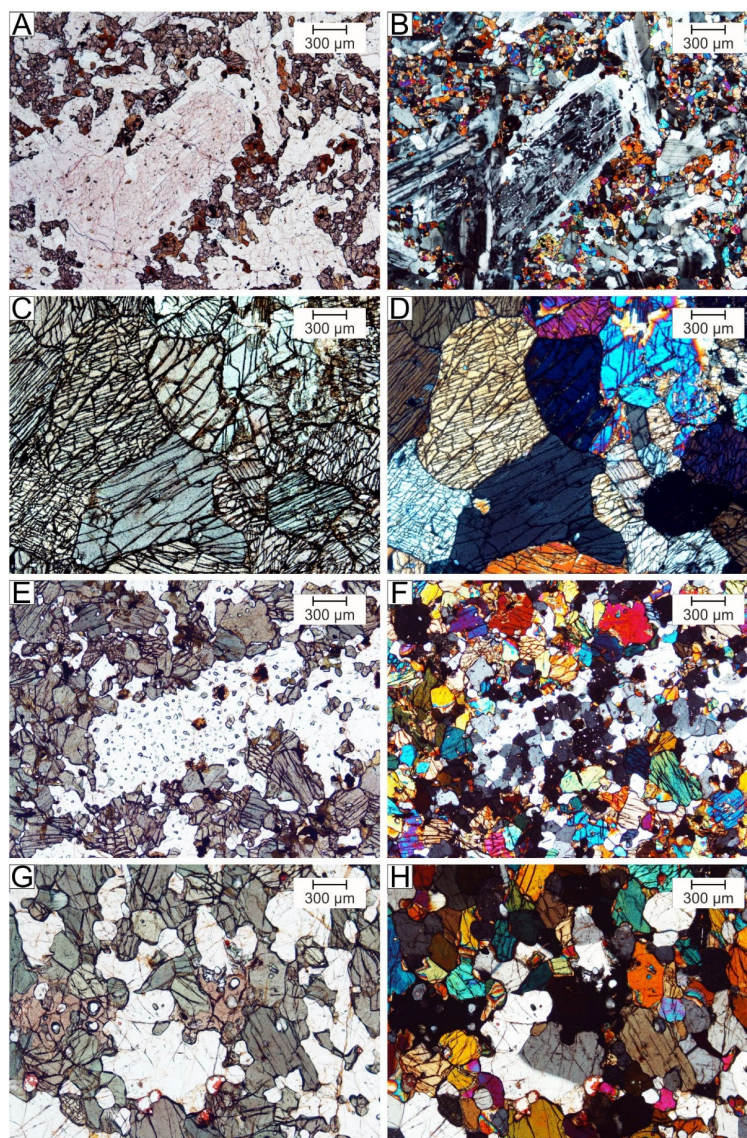


Figure 7. Photomicrographs of dolerite and related rocks (thin sections). (A,B) dolerite; (C,D) monomineral pyroxenite with large plagioclase laths replaced by nepheline in the center and fine-grained aggregates of clinopyroxene (purple), pargasite and biotite (brown); (E,F) nepheline-fassaite rock with nepheline pseudomorphs after plagioclase; (G,H) skarned pyroxenite with fassaite (brownish-tobacco green), nepheline (white), and garnet (brownish-orange). (A,C,E,G) plane-polarized light; (B,D,F,H) cross polarized light.

3. Analytical Methods

Representative samples of pyroxenite and nepheline-fassaite rocks were analyzed for major, trace, and rare-earth elements. Major elements were determined by X-ray fluorescence spectrometry (XRF) at the Center for Geodynamics and Geochronology of the Institute of the Earth's Crust (Irkutsk, Russia). Trace elements and rare earths were determined by inductively coupled plasma mass spectrometry (ICP-MS) on an Agilent Technologies Agilent 7500ce analyzer (Santa Clara, CA, USA) at the Limnological Institute (Irkutsk, Russia), at the Analytical Center *Ultramikroanaliz* (analyst S. Panteeva). For ICP-MS, the samples were fused with LiBO_2 following the standard procedure. Calibrations were with internal and international standards G-2, GSP-2, JG-2, and RGM-1. Analytical accuracy was 0.5–1.0% for major oxides and up to 5% for trace elements and REE.

The mineralogy of pyroxenite and related rocks was analyzed in more than 400 grains of clinopyroxene, garnet, amphibole, nepheline, plagioclase, and some other minerals in polished thin sections. The analyses were performed at the Analytical Center for Mineralogical, Geochemical, and Isotope Studies of the Geological Institute (Ulan-Ude, Russia) by scanning electron microscopy with energy dispersive X-ray spectroscopy (SEM-EDS) on a LEO 1430 VP scanning electron microscope with an Oxford Inca Energy 350 spectrometer. The operation conditions for EDS were: 20 keV beam energy, 0.4 nA beam current, and 50 s spectrum live acquisition time. The results were checked against synthetic compounds and natural minerals: SiO_2 (O, Si), BaF_2 (F, Ba), $\text{NaAlSi}_3\text{O}_8$ (Na), $\text{MgCaSi}_2\text{O}_6$ (Mg,Ca), Al_2O_3 (Al), $\text{Ca}_2\text{P}_2\text{O}_7$ (P), KAlSi_3O_8 (K), Cr-met.(Cr), Mn met. (Mn), and Fe met. (Fe) Matrix correction was performed with the XPP algorithm as part of the built-in Inca Energy software.

The $\delta^{18}\text{O}_{\text{V-SMOW}}$ and $\delta^{13}\text{C}_{\text{V-PDB}}$ values were analyzed on a Finnigan MAT 253 mass spectrometer at the Geological Institute (Ulan-Ude). The results are quoted in δ -notation ($\delta = (R1/R2 - 1) \times 1000$, where R1 and R2 are the $^{13}\text{C}/^{12}\text{C}$ and/or $^{18}\text{O}/^{16}\text{O}$ ratios in the sample and the standard, respectively) in permil (‰) relative to V-PDB (for C) and V-SMOW (for O) standards. Carbonates were analyzed for oxygen and carbon isotopes. CO_2 was extracted from minerals at 60 °C during reactions with H_3PO_4 for 2–4 h. The data quality was assessed using international reference materials NBS-18 and NBS-19. The analytical errors for the $\delta^{18}\text{O}$ and $\delta^{13}\text{C}$ values were $\pm 0.05\text{‰}$ and $\pm 0.1\text{‰}$, respectively. Oxygen isotope composition was analyzed by the laser-fluorination method [26]. Samples were heated with a 100 W CO_2 laser in a BrF_5 atmosphere. The $\delta^{18}\text{O}$ values obtained in this study were checked against the international reference materials NBS-28 quartz (9.64‰; n = 10) and NBS-30 biotite (5.10‰; n = 15). Additionally, the UWG-2 garnet standard (5.89‰) was used in each run. The accuracy of $\delta^{18}\text{O}$ values of the samples, estimated by comparison with the analyses of reference samples and according to reproducibility of replica measurements, was within 0.2‰.

4. Major- and Trace-Element Chemistry of Pyroxenite and Nepheline-Pyroxene Rocks

In the variation diagrams (Figure 8, Supplementary Table S1), the Tazheran dolerites, beerbachites, nepheline-pyroxene rocks, and pyroxenites plot, respectively, within the fields of monzogabbro, gabbro, feldspar gabbro, and lowest- SiO_2 feldspar gabbro and peridotite. Their compositions vary in the series dolerite–beerbachite–pyroxenite–nepheline-pyroxene rock. Dolerite sample is the highest in Al_2O_3 and SiO_2 , the lowest in CaO (Figure 8A,C), and intermediate between pyroxenite and nepheline-pyroxene rock in total alkalis (Figure 8A,B). Total alkalis increase markedly from pyroxenite to nepheline-pyroxene samples while the increase in silica is moderate (Figure 8A). The CaO values increase toward pyroxenite and correlate with lower silica in the SiO_2 -CaO diagram (Figure 8C), but show more complex correlations with total alkalis (Figure 8B): positive in nepheline-pyroxene rocks and negative in pyroxenites. The most leucocratic nepheline-pyroxene samples (SE1275B and SE1273A) are the richest in alkalis and Al_2O_3 and the least magnesian (Figure 8C,D).

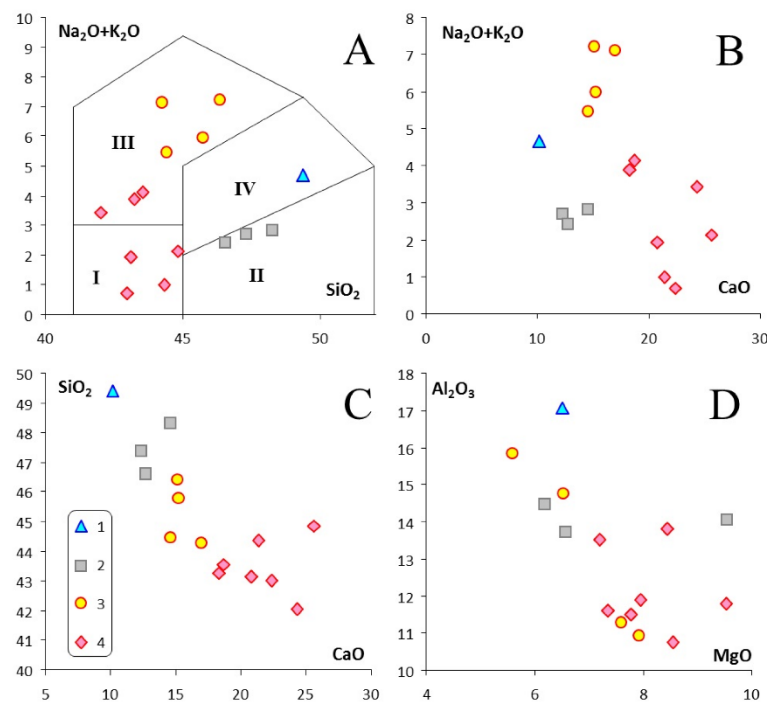


Figure 8. Tazheran rocks in variation diagrams. Fields of intrusive rocks in panel A are after [27], complemented by Lavrenchuk et al. [28]: I = peridotite, II = gabbro, III = feldspar gabbro, IV = monzogabbro. Dolerite (1), beerbachites (2), nepheline-fassaite rocks (3), pyroxenites (4). (A) $(\text{Na}_2\text{O}+\text{K}_2\text{O})\text{-SiO}_2$; (B) $(\text{Na}_2\text{O}+\text{K}_2\text{O})\text{-CaO}$; (C) $\text{SiO}_2\text{-CaO}$; (D) $\text{Al}_2\text{O}_3\text{-MgO}$.

The REE patterns (Figure 9) are relatively flat in most of pyroxenite (La_n/Yb_n from 1.6 to 2.9; $\Sigma\text{REE} = 61.2\text{--}85.9$ ppm) and beerbachite ($\text{La}_n/\text{Yb}_n = 2.2\text{--}3.2$; $\Sigma\text{REE} = 38\text{--}69.6$ ppm) samples but are the flattest in dolerites ($\text{La}_n/\text{Yb}_n = 1.3$; $\Sigma\text{REE} = 60.8$ ppm). The La_n/Yb_n ratios and ΣREEs are as high as 5.1 and 125.8 ppm, respectively, in pyroxenite sample SE827A (which is rich in alkalis, with 3.26 wt.% Na_2O), and in one nepheline-pyroxene sample (3.6 and 117.7 ppm, respectively).

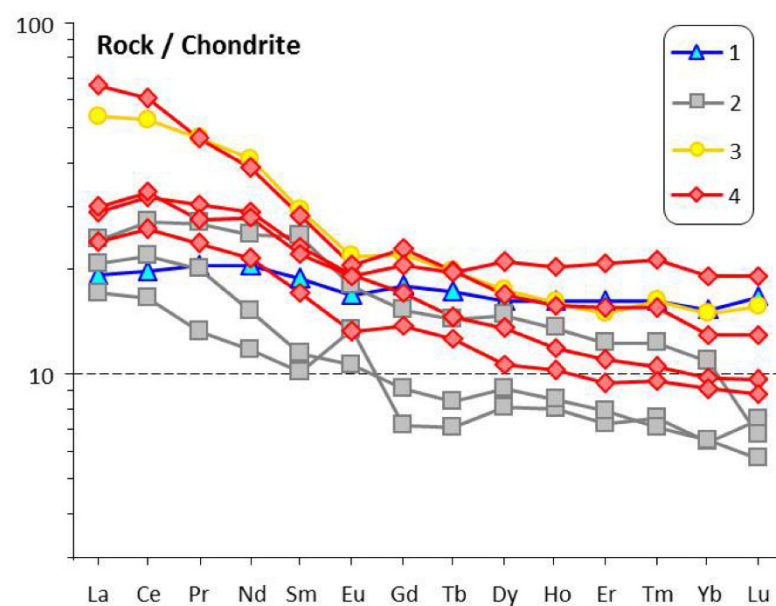


Figure 9. Chondrite-normalized REE spectra for pyroxenite and beerbachite. Color legend is the same as in Figure 8. Chondrite composition is after [29].

5. Mineralogy of Pyroxenite

The mineralogy of pyroxenite and nepheline-pyroxene rocks was analyzed in detail in several bodies, with a special focus on the body with remnant dolerite (Figure 6), which was sampled across at every 20–40 cm (SE1250c1 through SE1250c20): SE1250C, 1250c4, SE1250c11, and SE1250c12 in dolerite; SE1250A, SE1250c7, and SE1250c14 in pyroxenite; and SE1250c1, SE1250c2, SE1250c3, SE1250c5, SE1250c6, SE1250c4, SE1250c16, and SE1250c18 in garnet-bearing pyroxenite. Mineral chemistry was analyzed in samples of several relatively large pyroxenite bodies (SE827a, SE829a, SE1050c, and SE1252d), smaller bodies of garnet-bearing pyroxenite (SE1274a, SE1275b, and SE1523B), and one biotite-bearing pyroxenite body (SE1276b and SE1276c).

Clinopyroxene in the Tazheran samples can be classified as fassaite or late-generation diopside-hedenbergite pyroxene. Fassaite crystals look black macroscopically but are green (Figure 7C,D) or brown to reddish (Figure 7E,F) in thin sections, and are quite often pleochroic. Most of fassaites are euhedral or subhedral; some are zoned with lighter-color rims. The mineral contains 1–3 wt.% TiO_2 (Supplementary Table S2) and 5 wt.% to 13 wt.% Al_2O_3 in different samples (the difference within samples is commonly ≤ 4 wt.%). The Ti-Al contents are in positive correlation (Figure 10A), but no analyzed pyroxenes show a continuous trend; most of Al atoms are in the T site. Iron and magnesium vary as $X_{\text{Mg}} = 0.53$ –0.95 (Figure 10B). Most of analyses lie above the diopside-hedenbergite line in the Wo-En-Fs diagram (Figure 11), due to high Al contents. The diopside-hedenbergite compositions of pyroxene (Al_2O_3 4 wt.%; and $X_{\text{Mg}} = 0.6$ –0.7) are more common to dolerite, as well as in nepheline-rich samples (with lower alumina, which is mostly bound in nepheline).

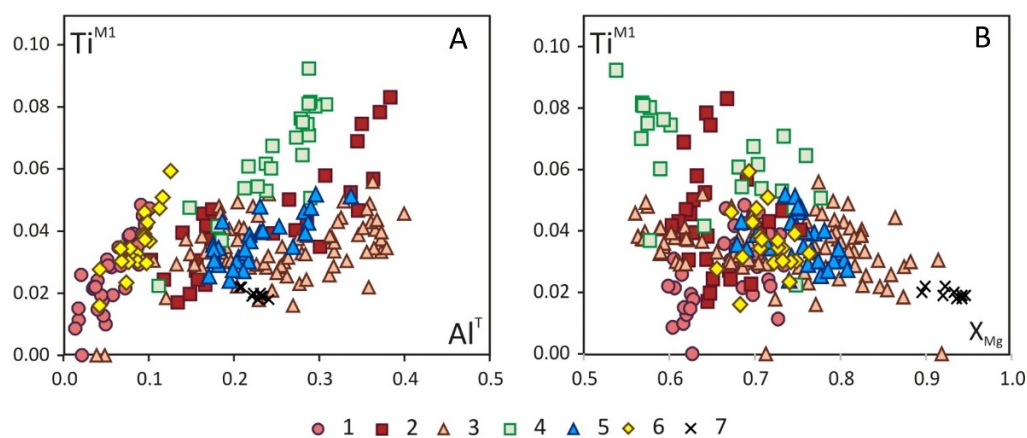


Figure 10. Pyroxene from pyroxenite in binary diagrams. 1–3 = pyroxenes from a pyroxenite fragment with remnant dolerite: dolerite (1), pyroxenite (2), garnet-bearing pyroxenite (3); 4–6 = pyroxenes from other pyroxenite fragments: pyroxenite (4), garnet-bearing pyroxenite (5), biotite-bearing pyroxenite (6); 7 = pyroxenes from the experiments of Mollo et al. [30]. (A) $\text{Ti}^{\text{M1}}-\text{Al}^{\text{T}}$; (B) $\text{Ti}^{\text{M1}}-X_{\text{Mg}}$.

Nepheline in pyroxenite and nepheline-fassaite samples occurs as isolated fine grains in interstices between fassaites and coarse (up to 1 cm) oikocrysts that enclose small fassaite grains. Such oikocrysts look like phenocrysts but appear as aggregates of finer anhedral grains in polarized-light images (Figure 7E,F). Dolerite-hosted nepheline occurs as fine aggregates with bitownite and spinel in the cores of relatively large plagioclase (labradorite) crystals (Figure 7A,B). Garnet-bearing rocks contain nepheline-clinopyroxene symplectites (Figure 12A). The percentage of kalsilite end-member (Ks) is most often between 15% and 20%, or sometimes 10–12% (Supplementary Table S3). Most of the analyzed nepheline grains contain 1–2 wt.% CaO.

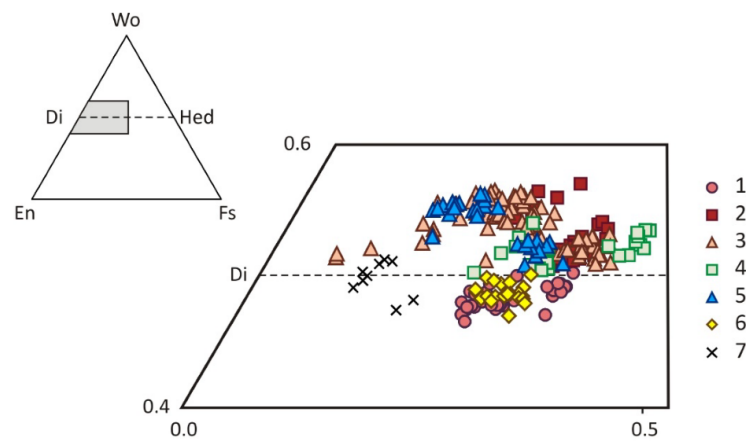


Figure 11. Pyroxene from pyroxenite in binary diagrams. 1–3 = pyroxenes from a pyroxenite fragment with remnant dolerite: dolerite (1), pyroxenite (2), garnet-bearing pyroxenite (3); 4–6 = pyroxenes from other pyroxenite fragments: pyroxenite (4), garnet-bearing pyroxenite (5), biotite-bearing pyroxenite (6); 7 = pyroxenes from the experiments of Mollo et al. [30].

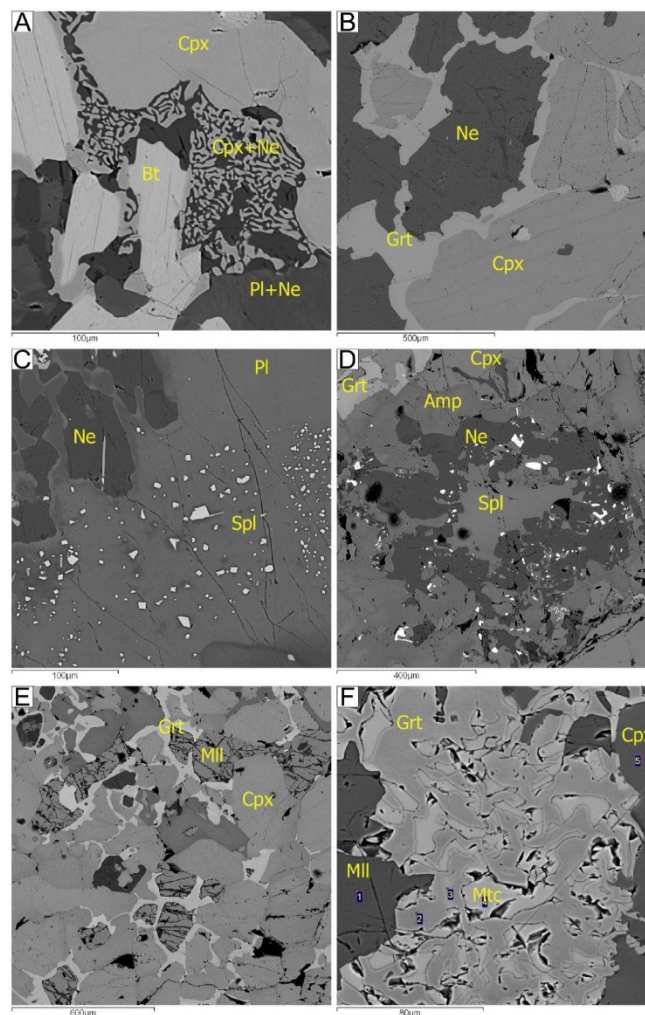


Figure 12. BSE images of dolerite and skarned pyroxenite. (A) nepheline-pyroxene symplectites between grains of pyroxene, biotite, and nephelized plagioclase in dolerite; (B) interstitial garnet between fassaite and nepheline grains; (C) small crystals of spinel in plagioclase from dolerite; (D) resorbed spinel in a nepheline coat; (E) interstitial garnet between fassaite and melilite grains; (F) garnet-monticellite symplectites between melilite and fassaite grains.

Amphibole corresponds to pargasite in all rock types (Figure 13), with 12–17 wt.% Al_2O_3 and $(\text{Na}_2\text{O}+\text{K}_2\text{O}) > 1$, in the A site. The percentage of amphibole in the samples is minor ($\leq 5\%$) to zero. The range of X_{Mg} is quite small in each of the analyzed samples but is generally from 0.28 to 0.82 (Supplementary Table S4). X_{Mg} in amphiboles of the dolerite-bearing fragment vary from 0.41 to 0.86.

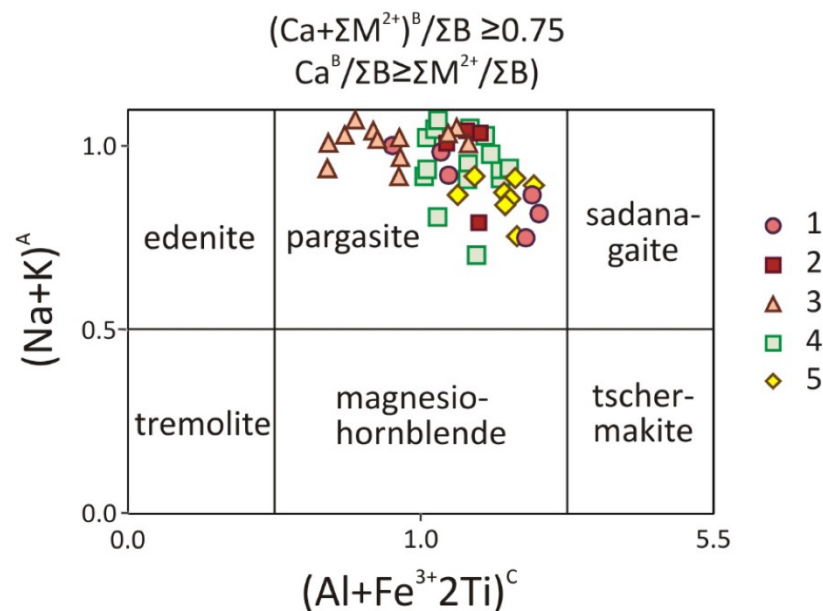


Figure 13. Amphiboles in $(\text{Na}+\text{K})^{\text{A}}-(\text{Al}+\text{Fe}^{3+}+2\text{Ti})^{\text{C}}$ diagram after [31]. 1–3 = amphiboles from dolerite (1), pyroxenite (2), and skarned pyroxenite (3) in the pyroxenite fragment with remnant dolerite; 4,5 = amphiboles from other pyroxenite fragments (4), including biotite-bearing pyroxenite (5).

Garnet is a typical mineral of later metasomatic reactions. It commonly occurs in rims of pyroxenite bodies or is interstitial between pyroxene and nepheline grains (Figure 12B), or sometimes forms clusters (Figure 7G,H). The grossular end-member reaches 60 to 85% (Supplementary Table S5), while the pyrospite end-member does not exceed 10% (rarely 12–17%) and is mainly of almandine composition (Figure 14). TiO_2 is from 0 to 1.5 wt.%. Zonation is weak to absent.

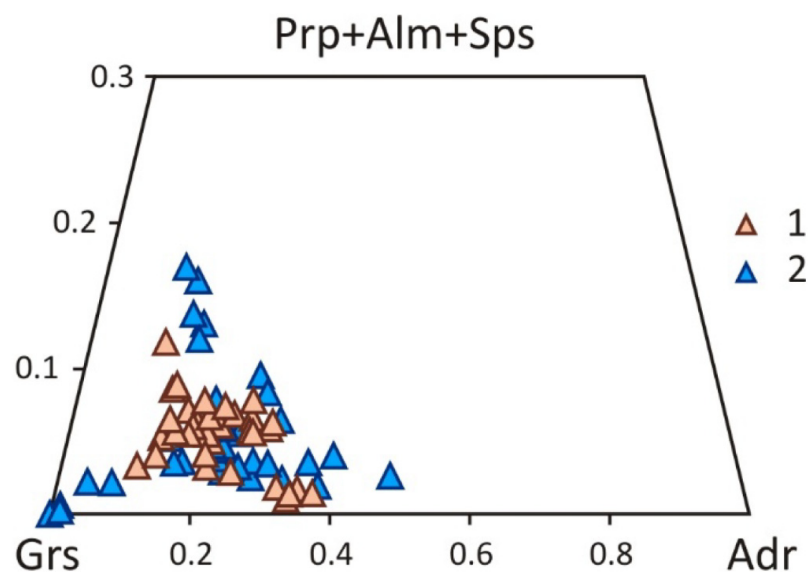


Figure 14. Garnets from skarned pyroxenite. 1 = garnets from pyroxenite fragment with remnant dolerite; 2 = garnets from other pyroxenite fragments.

Olivine is restricted to dolerite where it is a fine-grained matrix mineral coexisting with pyroxene, amphibole, and biotite among coarse plagioclase laths. It has a hyalosiderite composition (Supplementary Table S6) with moderate variations of X_{Mg} within 0.40–0.48.

Biotite occurs in remnant dolerite and in one skarned pyroxenite fragment. Dolerite-hosted biotite contains 2.2–7.4 wt.% TiO_2 (Supplementary Table S7), the variations being possibly due to later thermal effects on dolerite. X_{Mg} is within 0.63–0.73. Biotite in skarned pyroxenite has less variable and slightly higher TiO_2 (5.9 to 7.8 wt.%) and moderate X_{Mg} of 0.49–0.56. Some biotites contain 1–3 wt.% BaO.

Spinel exists as micrometer-sized light green crystals enclosed in coarse particles of nephelized plagioclase in dolerite (Figure 12C), or as coarse resorbed grains with nepheline rims in garnet-bearing pyroxenite (Figure 12D). Spinel has a homogeneous composition corresponding to pleonast (Supplementary Table S6), with $X_{Mg} = 0.31$ –0.33.

Plagioclase is likewise restricted to remnant dolerite where it has andesine or labradorite compositions (Supplementary Table S8). Some plagioclase laths enclose autometamorphic bitownite, either in rims of coarse laths or as spots of fine spinel grains.

Melilite occurs as euhedral or less often subhedral grains coexisting with garnet, fassaite, and nepheline (Figure 12E) in pyroxenite near the contact with marbles. Its composition corresponds to the Na-melilite ($CaNaAlSi_2O_7$ -50–60 %)-akermanite ($Ca_2MgSi_2O_7$ -30–40 %) series (Supplementary Table S9). The percentage of helenite ($Ca_2Al_2SiO_7$) is 1 to 11 %. According to the relative contents of cations Al (+ Fe^{3+}), Mg and Fe^{2+} , all melilite from garnet-bearing pyroxenite samples can be classified as alumoakermanite [32]. The contents of Na_2O reaching 6.9 wt.% approach the maximum values reported for both natural [33] and synthetic [34] melilite varieties.

Monticellite is a late phase found in symplectites with garnet or less often with garnet and nepheline, between coarser fassaite and melilite grains (Figure 12F). The composition of monticellite fits the monticellite ($CaMgSiO_4$)-kirschsteinite ($CaFeSiO_4$) series, with X_{Mg} 0.65–0.67 (Supplementary Table S9) and 13.9–14.8 wt% FeO.

6. Stable Isotopes (O, C)

The oxygen and carbon isotope compositions in minerals from different samples were analyzed relative to seawater (SMOW) and belemnite (PDB) standards, respectively (Table 1). The $\delta^{18}O_{SMOW}$ values in plagioclase and groundmass of the least altered dolerite are, respectively, 8.0 ‰ and 6.2 ‰ and are heavier in beerbachite and remnant dolerite from pyroxenite, as well as in pyroxenite main minerals. The $\delta^{18}O_{SMOW}$ enrichment in the latter increases in the series biotite → clinopyroxene → nepheline → carbonate, which indicates the lack of equilibrium between oxygen atoms in minerals, along with isotope fractionation between mineral pairs calculated for a large temperature range (Table 1). Note that $\delta^{18}O_{SMOW}$ in clinopyroxene from pyroxenite is similar to that from marble veins [35]. The level of $\delta^{18}O_{SMOW}$ and $\delta^{13}C_{PDB}$ in carbonate from pyroxenite is lower than in that from marble veins near the pyroxenite-marble contact (samples T-5, T-20, and T-22). The country rock marble carbonates have higher $\delta^{18}O_{SMOW}$ and $\delta^{13}C_{PDB}$ values.

Table 1. Oxygen and carbon isotope compositions in minerals from the Tazheran rocks and marbles.

Sample	Rock	Mineral	$\delta^{13}C$ ‰ _{v-PDB}	$\delta^{18}O$ ‰ _{v-SMOW}	$\Delta^{18}O_{cc-min}$	T (°C)
T-9p	Dolerite	Plagioclase		8.0		
		groundmass		6.2		
T-8	Remnant dolerite	groundmass		10.9		
T-8a				10.3		
T-6	Beerbachite	groundmass		10.3		

Table 1. Cont.

Sample	Rock	Mineral	$\delta^{13}\text{C}$ ‰V-PDB	$\delta^{18}\text{O}$ ‰ V-SMOW	$\Delta^{18}\text{O}_{\text{cc-min}}$	T (°C)
T-10	Pyroxenite	pyroxene		10.3	1.4	1038
		nepheline		11	0.7	1245
		biotite		9.2	2.5	568
		carbonate	−0.5	11.7		
T-5			−0.1	13.3		
T-20	Marble (veins, Tazheran)	carbonate	−0.1	17.7		
T-22			0.3	15.6		
T-13	Marble (country rock)	carbonate	−0.6	23.7		
T-14			2.3	27.5		

Note. Isotopic temperatures were calculated using calcite-diopside, calcite-nepheline [36], and calcite-phlogopite [37] isotope fractionation trends.

7. Discussion

The Tazheran pyroxenite and nepheline-pyroxene rocks would appear to perfectly comply with the model of metasomatism at the contact of silicate rocks and marbles in mineral assemblages and mineral chemistry. The minerals they contain are common to skarn assemblages: predominant fassaite, 0% to 50% nepheline, frequent andradite-grossular garnet and diopside-hedenbergite pyroxene, rare scapolite and monticellite, and occasional biotite (found in a single sample). However, the previous approach [13] of fitting all metasomatic diversity into a simple succession of contact metasomatic effects of cooling syenite magma on the country rocks and numerous xenoliths in a changing fluid environment, left overlooked many unusual and fascinating facts, including the existence of pyroxenite and nepheline-pyroxene rocks. The hypothesis of Konev and Samoilov [13], that pyroxenite (which they called *pyroxenolith*) would form by metasomatism of mafic hornfels (beerbachite) by fluids derived from syenite magma at the contact with carbonate xenoliths, is inconsistent with geological and petrological evidence.

Although being a whole unit tectonically, the Tazheran complex is an intricate mixture of gabbro (two types), syenite, and nepheline syenite units in terms of petrology. There were several intrusion events during the 470–457 Ma time span. Syenite and medium-Ti dolerite (converted to beerbachite) were the earliest: they have similar 471 ± 5 Ma U-Pb zircon [15] and U-Pb baddeleyite ages, respectively. Later episodes produced the 466 ± 2 Ma (tazheranite, U-Pb) forsterite-spinel calc-silicate vein [23] and 462.8 ± 2.5 Ma (perovskite, U-Pb) forsterite-diopside-phlogopite calc-silicate [38] rocks, and subalkaline gabbro, presumably 461 ± 2 Ma, as extrapolated from compositionally similar gabbro in the Okhon terrane [22,28,39]. Finally, nepheline syenite emplaced the latest, according to its 464–451 Ma U-Pb zircon age [15]. Note, however, that the latter young zircons were isolated from pegmatitic nepheline syenite which probably formed late during the process and thus hardly can be representative of the whole intrusion event. Carbonate rocks, often found as veins in syenite, likewise may be injection bodies [21], though their chemistry and mineralogy misfit the composition of mantle-derived carbonatite (see below). More likely, there were several batches of syenite and mafic magma coming from different chambers.

Another point is that the magma emplaced in the 600–650 °C middle crust at 4–5 kbar [40] during active strike-slip faulting [18]. The Tazheran complex has neither intrusive contacts with the country rocks nor signatures of metasomatism in calcite marble adjacent to syenite and gabbro. The syenite and mafic rocks along the margins are distinctly gneissic, as well as the silicate country rocks, which is evidence of ductile flow. Therefore, static magma crystallization, with formation of classical metasomatic zoning at the carbonate/silicate boundary [3,41–43] is inapplicable to this case.

The model that evokes the effect of fluids derived from intruding syenite magma on carbonate xenolith material [13] does not work either, for several reasons. First, the ~1 km

length of the “xenolith” (Figure 4) is poorly consistent with the small 6 km² size of the Tazheran complex. Second, neither the location of the carbonate body in the middle of the complex, near the southern boundary with the large field of beerbachite (metadolerite), nor its elongate geometry (Figure 3), match the concept of a ‘xenolith’. Third, the well exposed northern pyroxenite/beerbachite contact is sharp and free from signatures of metasomatism in beerbachite or mineralogical zoning in pyroxenite. Furthermore, the syenite bodies have no direct contacts with pyroxenite in the north and the surrounding beerbachites lack any metasomatic signatures.

Finally, the xenolithic nature of carbonate material in the magma chamber is disproved by the existence of a 10 m to 70 m thick marble zone near the contact with pyroxenite, which includes numerous pyroxenite fragments of different sizes and shapes from angular to round, elongate, or quasi-isometrical (Figure 5). Note also that the carbonate country rocks differ compositionally from their counterparts inside the Tazheran complex. Only calcite marbles are present among metamorphic rocks near the intrusions but dolomitic or dolomite-calcitic marbles occur 3–4 km away. At the same time, brucite marbles occur in abundance in the southern part of the complex as large blocks or numerous veins in syenite and subalkaline gabbro. Their origin was related [13] to the classical conversion of dolomite to periclase marble by thermal metamorphism and subsequent hydration with formation of brucite pseudomorphs after periclase. However, the presence of brucite marble veins piercing syenite and subalkaline gabbro [15,21] casts doubt on this mechanism, though details of the issue are beyond our consideration. Furthermore, dolomite-bearing calcite marbles coexist with pyroxenite in the metamorphic zone only. In this respect, their formation mechanism has implications for the genesis and protolith of pyroxenite.

The pyroxenite protolith was identified due to the discovery of remnant dolerite and the reconstruction of its successive metamorphic changes. The Tazheran dolerite appears as up to 2 m long lenses, which preserve ophitic textures with a matrix of plagioclase laths (Figure 7D) in the middle of a well exposed and relatively large pyroxenite body among marbles. The oxygen isotope composition of plagioclase and the least altered dolerite groundmass approaches the values typical of igneous rocks [44]. On the other hand, the features of melanocratic minerals, such as olivine, diopside-hedenbergite Ti-pyroxene, pargasite, and high-Ti biotite, may be traces of high-temperature (automagmatic) recrystallization. This hypothesis is supported by the presence of thin (2–3 mm) veins composed of the same melanocratic minerals compositionally similar to those of the groundmass. Superposed metasomatic processes left a record in plagioclase, which has been partly replaced by nepheline and contains fine spinel inclusions (Figure 7A,B and Figure 12C). Dolerite converted to pyroxenite still preserves a visible ophitic texture but its plagioclase laths are fully replaced by nepheline aggregates (Figure 7E,F). Furthermore, higher $\delta^{18}\text{O}$ values in altered dolerite relative to that in fresher varieties indicate isotope re-equilibration under the effect of metasomatic fluids more enriched with ^{18}O . The pyroxenite body is skarned along the margins, with formation of grossular-andradite garnet, diopside-hedenbergite pyroxene, or less often scapolite, melilite, or monticellite.

The pyroxenite-hosted dolerite (like pyroxenite itself) shares chemical similarity with beerbachite from the large field in the northern Tazheran complex (Figure 4) and borders the zone of pyroxenite with marble in the south. Beerbachite may result from high-temperature metamorphism (autometamorphism) of dolerite and contains its weakly altered remnants. The two rock types have similar major- and trace-element chemistry and REE patterns (Figure 9). Thus, phase 1 dolerite, which intruded quasi-synchronously with syenite about 470 Ma ago, may be the protolith of both pyroxenite and beerbachite.

The carbonate rocks of the Tazheran area would be interpreted as related to carbonatite (e.g., proceeding from abundance of pyroxenite fragments) but for their mineralogy and chemistry rather corresponding to sedimentary origin. Namely, such features as moderate contents of REEs or other trace elements common to carbonatite, as well as $\delta^{18}\text{O}$ and $\delta^{13}\text{C}$ values different from those in both mantle-derived rocks and the country rock marble (Table 1), are inconsistent with the criteria of mantle-derived carbonatite [45]. The only

reasonable explanation for the presence of pyroxenite fragments among the marbles would lie with uptake of country rock fragments by a ductile carbonate flow during the formation of marbles. However, the latter are coarse-grained and free from any signatures of ductile flow. The paradoxical combination of the “intrusive” appearance and “sedimentary” compositions of the carbonate rocks may result from melting of sedimentary protoliths in the lower crust. Geoscientists are usually skeptical about melting of carbonates in the crustal conditions bearing in mind that their melting point of $>1200\text{ }^{\circ}\text{C}$ determined experimentally [46] far exceeds crustal temperatures. However, calcite can melt at $\sim 700\text{ }^{\circ}\text{C}$ in vapor-saturated conditions (Figure 15A,B [45]), and the melting point for dolomite (Figure 15C,D) is as low as $\sim 600\text{ }^{\circ}\text{C}$ [47]. The silicate systems behave in exactly the same way: the dry and wet liquidus may be $200\text{--}300\text{ }^{\circ}\text{C}$ different. Therefore, anatectic melting of carbonates in the lower crust must be as widespread as anatexis and melting of granites at $650\text{--}700\text{ }^{\circ}\text{C}$. Meanwhile, there have been few reports on carbonates that would bear signatures of intrusive-like relations with the country rocks and show sedimentary affinity in compositions [21,48–53]. Such reports are rare because geologists commonly explain the unusual relationships between carbonate and silicate rocks by ductile squeezing of carbonates into a more competent silicate matrix rather than by melt intrusion, and partly because this explanation requires quite narrow $\text{H}_2\text{O}/(\text{CO}_2 + \text{H}_2\text{O})$ ranges in the melting region. Melting of calcite under crustal temperatures ($<800\text{ }^{\circ}\text{C}$) is possible at $\text{CO}_2/(\text{CO}_2+\text{H}_2\text{O})$ from 0.4 to 0.6, and the respective range for dolomite is 0.02–0.06. Deep-crustal anatectic melting of originally sedimentary carbonates, with participation of local or regional-scale inputs of aqueous fluids, appears realistic. Correspondingly, the Tazheran dolomite-bearing calcite marble may result from such melting and subsequent emplacement at shallower depths in the middle crust.

The possibility of the anatectic melting of carbonates was justified for originally sedimentary carbonate rocks [54] from Yates Prospect, Otter Lake, Quebec (Central Metasedimentary Belt of the Grenville Province). On the other hand, an earlier pegmatite-related pneumatolytic model [54] invoked skarn formation leading to marble melting (i.e., limestone “syntexis”). Both models require H_2O inputs into carbonates, but the model of Lentz [55], unlike that of Schumann et al. [54], ties the melting of sedimentary carbonates to a specific syenite body.

Judging by their spatial coexistence with dolomite-bearing calcite marble, the Tazheran pyroxenite may have formed by joint contribution of carbonate material and mafic magma. Both beerbachite and pyroxenite south of it most likely were derived from phase 1 dolerite and differ from their precursor rock in higher contents of calcium, low silica, and large ranges of alkalis (Figure 8). This composition of pyroxenite (and pyroxene-nepheline rocks) may result either from assimilation of carbonate material by mafic melts or from an effect of carbonated fluids on previously crystallized dolerite. The first explanation appears to be more realistic and can account for many facts.

The state of carbonate material supplied to the mafic melt is critical in this respect. Data from the Hortavaer complex [56] showed that melt contamination with solid carbonate would be piecemeal, whereas assimilation of low-viscosity, carbonate-rich melts would be pervasive. As was found out experimentally [30], the crystallization degree of the basalt-carbonate mixture at $1200\text{ }^{\circ}\text{C}$ can increase from 1% for purely basaltic composition to 60% in the presence of 20% of calcite, i.e., the carbonate input increases the liquidus of the hybrid melt. However, it was shown long ago [57] that the melt cannot dissolve xenoliths, increasing its liquidus. Therefore, assimilation of carbonate material (5–10%), if the marbles belonged to the roof [13], is very unlikely, more so pyroxenite lacks carbonate xenoliths.

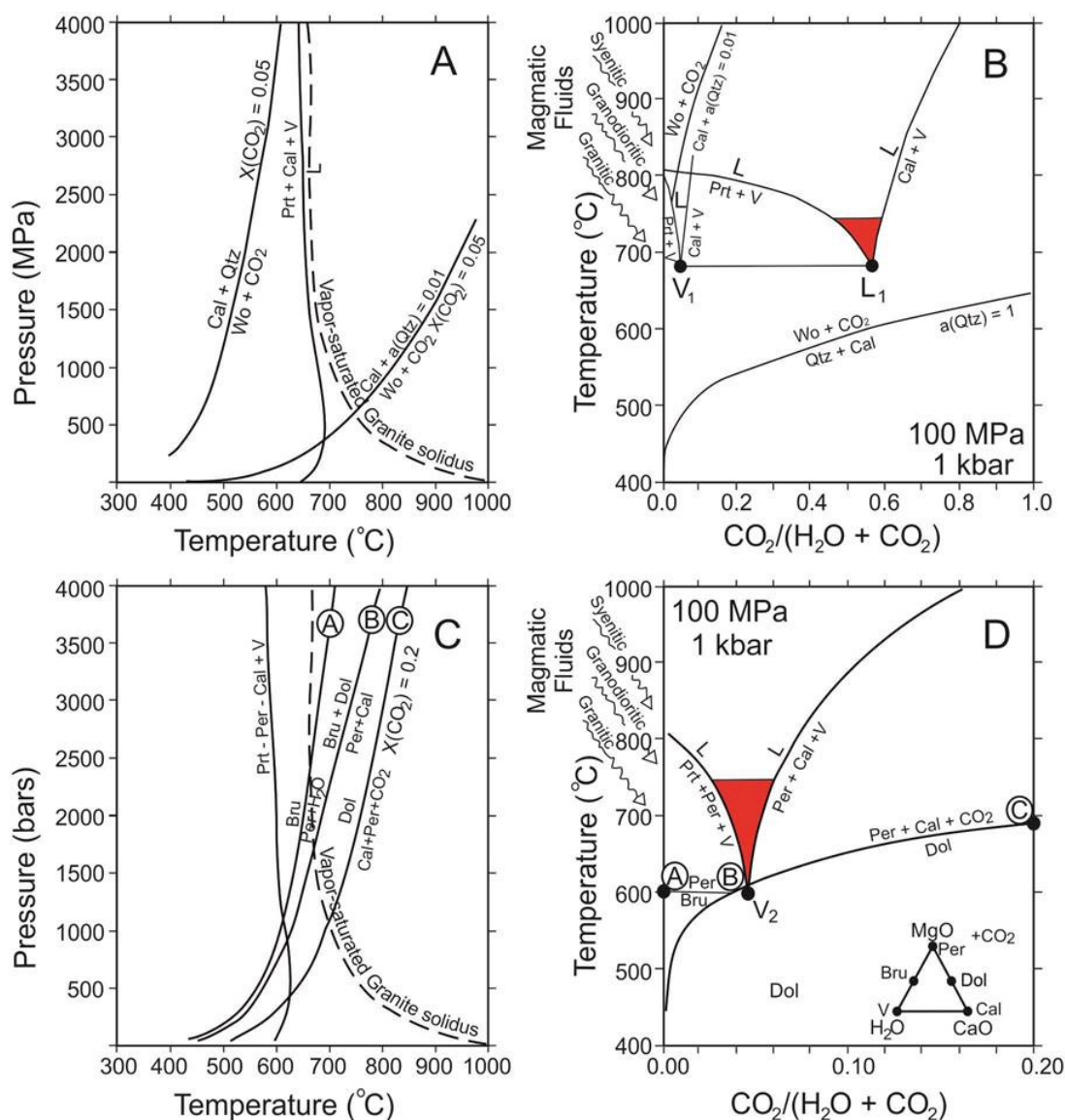


Figure 15. (A,C) Pressure vs. temperature diagram; (B,D) temperature vs. $X(\text{CO}_2)$ diagram for CaO-CO₂-H₂O (A,B) and MgO-CaO-CO₂-H₂O (C,D) systems, after [55]. Panels (A,B) illustrate calcite + quartz → wollastonite + CO₂ decarbonation reaction (at an $X(\text{CO}_2) = 0.05$ in (A) and a quartz activity ($a(\text{Qtz})$) of 1 and 0.01 (in solution) relative to portlandite-calcite-vapor-liquid (melt) eutectic (CaO-CO₂-H₂O system [46], and the vapor-saturated granite solidus. Cal = calcite, Prt = portlandite, Qtz = quartz, V = vapor (fluid), and L = liquid (melt). Panels (C,D) illustrate decarbonation reaction dolomite → periclase (or brucite) + calcite + CO₂ (at a $X(\text{CO}_2) = 0.05$ in (A) relative to portlandite-calcite-periclase-vapor-liquid (melt) eutectic (MgO-CaO-CO₂-H₂O system [47], and the vapor-saturated granite solidus. Dol = dolomite, Per = periclase, Bru = brucite, Cal = calcite, Prt = portlandite, V = vapor (fluid), and L = liquid (melt). Red region corresponds to crustal conditions in which melting is possible.

According to the experiments of Mollo et al. [30], pyroxene which crystallizes from mafic magma containing 5% to 20% of assimilated calcite or dolomite has a fassaitic composition with 5–9 wt.% Al₂O₃, while the residual melt (Figure 16) may change composition in different ways depending on the amount of assimilated carbonate and the presence of aqueous fluid.

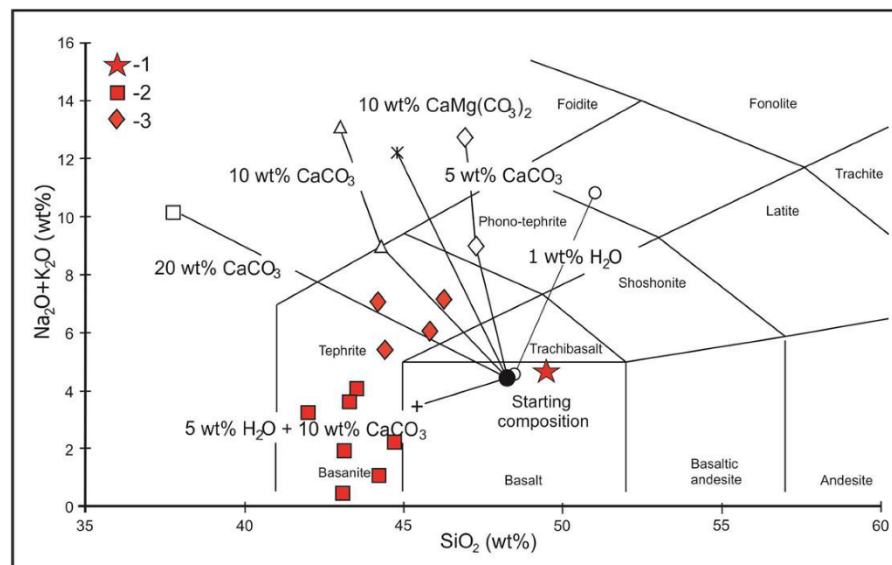


Figure 16. Residual glasses from experiments of Mollo et al. [30] and Tazheran samples in TAS diagram. 1 = dolerite; 2 = pyroxenite; 3 = nepheline-fassaite rock.

Total alkalis may either increase or decrease in different experimental conditions, whereas SiO_2 almost always decreases. These results appear to be applicable to the Tazheran pyroxenite: the Al_2O_3 range in most of pyroxenes we analyzed fits perfectly the 5 to 9 wt.% range (Figure 10), while the nepheline-Ti-fassaite sites in pyroxenite may be zones of alkali- and LREE-rich residual melt after crystallization of pyroxene. Alternatively, the mafic melt can be unevenly contaminated with carbonate material [30] and become either enriched or depleted in alkalis. In this case, the dolerite bodies may be the crystallized batches of non-contaminated mafic magma. The magmatic origin of pyroxenite does not rule out later metasomatic reactions in the cooling magmatic system which could produce typical skarn assemblages with garnet, melilite, diopside-hedenbergite pyroxene, etc. The presence of numerous pyroxenite fragments among marbles can be explained in this context by concurrent intrusion of contaminated mafic and carbonate melts. As the magmatic system was cooling down, the pyroxenite that crystallized at markedly higher temperatures before the carbonate melt could break down into fragments which became entrained with the melt.

Although known as a skarn mineral [10], fassaite can also crystallize from a melt, as it was reported in many publications on carbonate assimilation by silicate magma [5,6,8,58,59]. However, the Tazheran case is rare or even unique: the batches of contaminated pyroxenitic melt, which can crystallize with formation of fassaite or nepheline-fassaite rocks, existed and intruded independently rather than making a mottled pattern of “isles” among noncontaminated silicates.

On the other hand, the purely metasomatic origin of pyroxenite due to the action of a hydrous carbonate melt (fluid) on beerbachite cannot be fully rejected. This mechanism even would be more probable if the Tazheran pyroxenite existed only as fragments among marbles rather than making a 70 m wide long zone (Figure 4). Moreover, the pyroxenite zone has a sharp boundary with that of beerbachite in its north and lacks later metasomatic signatures, unlike the skarned pyroxenite fragments in marbles. Note that this part of the area is almost 100% exposed, unlike the western part, where pyroxenite and marble were mapped from sporadic outcrops and scattered eluvium.

8. Conclusions

The pyroxenite and nepheline-pyroxene rocks of the Tazheran complex occur in a long continuous zone between beerbachites (produced by thermal metamorphism of tholeiitic dolerites) and dolomite-bearing calcite marbles, or as mm to n·10 m fragments among

the marbles. Pyroxenes in these rocks have fassaitic compositions with 5–13 wt.% Al_2O_3 , 1–3 wt.% TiO_2 , and 0.6–0.7 X_{Mg} . The compositions of the pyroxenites, as well as their relations with the surrounding rocks, are poorly consistent with a purely metasomatic origin, though metasomatism did occur while the whole system was cooling down, and led to the formation of mineral assemblages with grossular-andradite garnet or, less often, with scapolite, mellilite, or phlogopite. The Tazheran rocks appear rather to provide the most spectacular record of crust-mantle interactions within the Olkhon collisional system. Intrusion of mantle-derived mafic melts into thick crust impregnated with fluids caused partial melting of the heterogeneous carbonate-silicate substrate and the formation of the respective melts. Early (?) during the event, the interaction of carbonate and mafic melts produced a contaminated hybrid pyroxenitic melt mixture. The viscous thick crust was tight for ascending mantle and crustal melts, but concurrent emplacement of compositionally different magma batches at shallower depths was possible through local permeable zones resulting from strike-slip faulting and formation of pull-apart structures. Roughly synchronous injections of mafic, pyroxenitic, and carbonate melts led to silicate-carbonate mixing and crystallization of pyroxenite with fassaitic pyroxenes. The ascending hydrous carbonate melt having a lower crystallization temperature entrained the fragments of pyroxenite, which crystallized previously at a higher temperature.

Supplementary Materials: The following are available online at <https://www.mdpi.com/article/10.3390/min11060654/s1>, Table S1: Whole-rock major oxide (wt%) and some trace element (ppm) in dolerite, pyroxenite and beerbachite; Table S2: Mineral chemistry of pyroxenes from dolerite, pyroxenites and garnet-bearing pyroxenites, Table S3: Mineral chemistry of nephelines from dolerite, pyroxenites and garnet-bearing pyroxenites; Table S4: Mineral chemistry of amphiboles from dolerite, pyroxenites and garnet-bearing pyroxenites; Table S5: Mineral chemistry of garnets from garnet-bearing pyroxenites; Table S6: Mineral chemistry of olivine from dolerite; Table S7: Mineral chemistry of biotites from dolerite and Bt-bearing nepheline-pyroxenite; Table S8: Mineral chemistry of plagioclases from dolerite; Table S9: Mineral chemistry of melilite and monticellite from garnet-bearing pyroxenites.

Author Contributions: E.V.S.: conceptualization, geological study, sampling, data interpretation, preparation of tables and figures, writing the manuscript; A.V.L.: geological study, sampling, preparation of some figures and tables, writing a part of the manuscript (major- and trace-element chemistry); A.E.S.: geological study, sampling, preparation of some figures and tables, writing a part of the manuscript (mineralogy); A.G.D.: isotopic analyses, writing a part of the manuscript; S.V.K.: analyses of minerals, writing a part of the manuscript (analytical methods). All authors have read and agreed to the published version of the manuscript.

Funding: The study was carried out on government assignments to Institute of the Earth's Crust (Irkutsk) and Institute of Geology and Mineralogy (Novosibirsk). Geological and geochemical investigations were supported by the Russian Foundation for Basic Research (Project 20-05-00005). Mineral chemistry was analyzed under the support of the government of the Russian Federation (Project 075-15-2019-1883).

Acknowledgments: We wish to thank T. Perepelova, O. Sklyarova and I. Barash for assistance in manuscript preparation. Thoughtful comments by three anonymous reviewers on this manuscript are gratefully acknowledged.

Conflicts of Interest: The authors declare no conflict of interest.

References

1. Yardley, B.W.; Kerrick, D.M. Contact Metamorphism. Washington DC (Mineralogical Society of America: Reviews in Mineralogy, Vol. 26), 1992, xvi+ 847 pp. Price \$26.00. *Mineral. Mag.* **1993**, *57*, 359–360. [[CrossRef](#)]
2. Meinert, L.D. Skarns and skarn deposits. *Geosci. Can.* **1992**, *19*, 145–162. [[CrossRef](#)]
3. Meinert, L.D. Igneous petrogenesis and skarn deposits. *Geol. Assoc. Can. Spec.* **2016**, *40*, 569–583.
4. Freda, C.; Gaeta, M.; Misiti, V.; Mollo, S.; Dolfi, D.; Scarlato, P. Magma-carbonate interaction: An experimental study on ultrapotassic rocks from Alban Hills (Central Italy). *Lithos* **2010**, *101*, 397–415. [[CrossRef](#)]
5. Iacono-Marziano, G.; Gaillard, F.; Pichavant, M. Limestone assimilation by basaltic magmas: An experimental re-assessment and application to Italian volcanoes. *Contrib. Mineral. Petrol.* **2008**, *155*, 719–738. [[CrossRef](#)]

6. Gaeta, M.; Di Rocco, T.; Freda, C. Carbonate assimilation in open magmatic systems: The role of melt-bearing skarns and cumulate-forming processes. *J. Petrol.* **2009**, *50*, 361–385. [[CrossRef](#)]
7. Di Rocco, T.; Freda, C.; Gaeta, M.; Mollo, S.; Dallai, L. Magma chambers emplaced in carbonate substrate: Petrogenesis of skarn and cumulate rocks and implications for CO₂ degassing in volcanic areas. *J. Petrol.* **2012**, *53*, 2307–2332. [[CrossRef](#)]
8. Ganino, C.; Arndt, T.; Chauvel, C.; Jean, A.; Athurion, C. Melting of carbonate wall rocks and formation of the heterogeneous aureole of the Panzhihua intrusion, China. *Geosci. Front.* **2013**, *4*, 535–546. [[CrossRef](#)]
9. Morimoto, N.; Fabries, J.; Ferguson, A.K.; Ginzburg, I.V.; Ross, M.; Seifert, F.A.; Zussman, J.; Aoki, K.; Gottardi, G. Nomenclature of pyroxenes. *Am. Mineral.* **1988**, *73*, 1123–1133.
10. Deer, W.A.; Howie, R.A.; Zussman, J. *Rock-Forming Minerals. Volume 2A. Single-Chain Silicates*; The Geological Society: London, UK; Alden Press: Oxford, UK, 1997; p. 668.
11. Gilg, H.A.; Lima, A.; Somma, R.; Belkin, H.E.; De Vivo, B.; Ayuso, R.A. Isotope geochemistry and fluid inclusion study of skarns from Vesuvius. *Miner. Petrol.* **2001**, *73*, 145–176. [[CrossRef](#)]
12. Wenzel, T.; Baumgartner, L.P.; Brugmann, G.E.; Konnikov, E.G.; Kislov, E.V.; Orsoev, D.A. Contamination of mafic magma by partial melting of dolomitic xenoliths. *Terra Nova* **2001**, *13*, 197–202. [[CrossRef](#)]
13. Konev, A.A.; Samoilov, V.S. *Contact Metamorphism and Metasomatism in the Aureole of the Tazheran Alkaline Intrusion*; Nauka: Novosibirsk, Russia, 1974; p. 246. (In Russian)
14. Fedorovsky, V.S.; Sklyarov, E.V.; Mazukabzov, A.M.; Kotov, A.B.; Kargopolov, S.A.; Lavrenchuk, A.V.; Starikova, A.E. *Geological Map of the Tazheran Massif*; Gruppa Kompanii A: Moscow, Russia, 2009.
15. Sklyarov, E.V.; Fedorovsky, V.S.; Kotov, A.B.; Lavrenchuk, A.V.; Mazukabzov, A.M.; Levitsky, V.I.; Salnikova, E.B.; Starikova, A.E.; Yakovleva, S.Z.; Anisimova, I.V.; et al. Carbonatites in collisional settings and pseudo-carbonatites of the Early Paleozoic Ol'khon collisional system. *Russ. Geol. Geophys.* **2009**, *50*, 1091–1106. [[CrossRef](#)]
16. Donskaya, T.V.; Sklyarov, E.V.; Gladkochub, D.P.; Mazukabzov, A.M. The Baikal collisional metamorphic belt. *Doklady Earth Sci.* **2000**, *374*, 1075–1079.
17. Donskaya, T.V.; Gladkochub, D.P.; Fedorovsky, V.S.; Sklyarov, E.V.; Cho, M.; Sergeev, S.A.; Demonterova, E.I.; Mazukabzov, A.M.; Lepekhina, E.N.; Cheong, W.; et al. Pre-collisional (0.5 Ga) complexes of the Olkhon terrane (southern Siberia) as an echo of events in the Central Asian Orogenic Belt. *Gondwana Res.* **2017**, *42*, 243–263. [[CrossRef](#)]
18. Fedorovsky, V.S.; Sklyarov, E.V. The Ol'khon Geodynamic Research Site (Baikal): High-Resolution Aerospace Data and Geological Maps of New Generations. *Geodyn. Tectonophys.* **2010**, *1*, 331–418, (in Russian with English abstract). [[CrossRef](#)]
19. Fedorovsky, V.S.; Sklyarov, E.V.; Gladkochub, D.P.; Mazukabzov, A.M.; Donskaya, T.V.; Lavrenchuk, A.V.; Starikova, A.E.; Dobretsov, N.L.; Kotov, A.B.; Tevelev, A.V. *Aerospace Geological Map of the Olkhon Region (Baikal, Russia)*; Copymaster Prof. Center: Moscow, Russia, 2017.
20. Fedorovsky, V.S.; Sklyarov, E.V.; Gladkochub, D.P.; Mazukabzov, A.M.; Donskaya, T.V.; Lavrenchuk, A.V.; Starikova, A.E.; Dobretsov, N.L.; Kotov, A.B.; Tevelev, A.V. Collision system of West Pribaikalie: Aerospace geological map of Olkhon region (Baikal, Russia). *Geodyn. Tectonophys.* **2020**, *11*, 447–452. [[CrossRef](#)]
21. Sklyarov, E.V.; Fedorovsky, V.S.; Kotov, A.B.; Lavrenchuk, A.V.; Mazukabzov, A.M.; Starikova, A.E. Carbonate and silicate-carbonate injection complexes in collision systems: The West Baikal region as an example. *Geotectonics* **2013**, *47*, 180–196. [[CrossRef](#)]
22. Whitney, D.L.; Evans, B.W. Abbreviations for names of rock-forming minerals. *Am. Mineral.* **2010**, *95*, 185–187. [[CrossRef](#)]
23. Fedorovsky, V.S.; Sklyarov, E.V.; Izokh, A.E.; Kotov, A.B.; Lavrenchuk, A.V.; Mazukabzov, A.M. Strike-slip tectonics and subalkaline mafic magmatism in the Early Paleozoic collisional system of the western Baikal region. *Russ. Geol. Geophys.* **2010**, *51*, 534–547. [[CrossRef](#)]
24. Starikova, A.E.; Sklyarov, E.V.; Kotov, A.B.; Salnikova, E.B.; Fedorovskii, V.S.; Lavrenchuk, A.V.; Mazukabzov, A.M. Vein calciphyre and contact Mg skarn from the Tazheran Massif (Western Baikal area, Russia): Age and genesis. *Doklady Earth Sci.* **2014**, *457*, 1003–1007. [[CrossRef](#)]
25. Sklyarov, E.V.; Karmanov, N.S.; Lavrenchuk, A.V.; Starikova, A.E. Perovskites of the Tazheran Massif (Baikal, Russia). *Minerals* **2019**, *9*, 323. [[CrossRef](#)]
26. Sharp, Z.D. A laser-based microanalytical method for the in situ determination of oxygen isotope ratios of silicates and oxides. *Geochim. Cosmochim. Acta* **1990**, *54*, 1353–1357. [[CrossRef](#)]
27. Middlemost, E.A.K. Naming materials in the magma/igneous rock system. *Earth Sci. Rev.* **1994**, *37*, 215–224. [[CrossRef](#)]
28. Lavrenchuk, A.V.; Sklyarov, E.V.; Izokh, A.E.; Kotov, A.B.; Sal'nikova, E.B.; Fedorovskii, V.S.; Mazukabzov, A.M. Compositions of gabbro intrusions in the Krestovsky Zone (Western Baikal Region): A record of plume-suprasubduction mantle interaction. *Russ. Geol. Geophys.* **2017**, *58*, 1139–1153. [[CrossRef](#)]
29. Boynton, W.V. Cosmochemistry of the rare earth elements: Meteorite studies. *Dev. Geochem.* **1984**, *2*, 63–114.
30. Mollo, S.; Gaeta, M.; Freda, C.; Di Rocco, T.; Misiti, V.; Scarlato, P. Carbonate assimilation in magmas: A reappraisal based on experimental petrology. *Lithos* **2010**, *114*, 503–514. [[CrossRef](#)]
31. Hawthorne, F.C.; Oberti, R.; Harlow, G.E.; Maresch, W.V.; Martin, R.F.; Schumacher, J.C.; Welch, M.D. Nomenclature of the amphibole supergroup. *Am. Mineral.* **2012**, *97*, 2031–2048. [[CrossRef](#)]

32. Wiedenmann, D.; Zaitsev, A.N.; Britvin, S.N.; Krivovechev, S.V.; Keller, J. Alumoakermanite, $(Ca, Na)_2(Al, Mg Fe^{2+})(Si_2O_7)$, a new mineral from the active carbonatite-nephelinite-phonolite volcano Oldonyo Lengai, Northern Tanzania. *Min. Mag.* **2009**, *73*, 373–384. [[CrossRef](#)]
33. Wiedenmann, D.; Keller, J.; Zaitsev, A.N. Melilite-group minerals at Oldoinyo Lengai, Tanzania. *Lithos* **2010**, *118*, 112–118. [[CrossRef](#)]
34. Yoder, H.S. Melilite stability and paragenesis. *Fortschr. Miner.* **1973**, *50*, 140–173.
35. Doroshkevich, A.; Sklyarov, E.; Starikova, A.; Vasiliev, V.; Ripp, G.; Izbrodin, I.; Posokhov, V. Stable isotope (C, O, H) characteristics and genesis of the Tazheran brucite marbles and skarns, Olkhon region, Russia. *Miner. Petrol.* **2016**, *115*, 153–169. [[CrossRef](#)]
36. Zheng, Y.F. Calculation of oxygen isotope fractionation in anhydrous silicate minerals. *Geochim. Cosmochim. Acta* **1993**, *57*, 1079–1091. [[CrossRef](#)]
37. Valley, J.W. Oxygen isotopes in zircon. *Rev. Mineral. Geochem.* **2003**, *53*, 343–385. [[CrossRef](#)]
38. Li, Q.; Li, X.; Liu, Y.; Wu, F.; Yang, J.; Mitchell, R.H. Precise U–Pb and Th–Pb age determination of kimberlitic perovskites by secondary ion mass spectrometry. *Chem. Geol.* **2010**, *269*, 396–405. [[CrossRef](#)]
39. Lavrenchuk, A.V.; Sklyarov, E.V.; Izokh, A.E.; Kotov, A.B.; Vasyukova, E.A.; Fedorovskii, V.S.; Gladkochub, D.P.; Donskaya, T.V.; Mazukabzov, A.M. Birkhin volcanoplutonic association, Ol’khon Region, Western Baikal Area: Petrological criteria of comagmatic origin. *Petrology* **2019**, *27*, 291–306. [[CrossRef](#)]
40. Sklyarov, E.V.; Lavrenchuk, A.V.; Fedorovsky, V.S.; Gladkochub, D.P.; Donskaya, T.V.; Kotov, A.B.; Mazukabzov, A.M.; Starikova, A.E. Regional contact metamorphism and autometamorphism of the Olkhon Terrane (West Baikal Area). *Petrology* **2020**, *28*, 47–61. [[CrossRef](#)]
41. Zharikov, A. Skarns. Parts I, II, III. *Intern. Geol. Rev.* **1970**, *12*, 541–559, 619–647, 760–775. [[CrossRef](#)]
42. Burt, D.M. Mineralogy and petrology of skarn deposits. *Soc. Ital. Mineral. Petrol. Rendic.* **1977**, *33*, 859–873.
43. Einaudi, M.T.; Meinert, L.D.; Newberry, R.I. Skarn deposits. *Econ. Geol.* **1981**, *12*, 327–391.
44. Hoefs, J. *Stable Isotope Geochemistry*; Springer Science & Business Media: Berlin, Germany, 2015; p. 404.
45. Mitchell, R.H. Carbonatites and carbonatites and carbonatites. *Can. Mineral.* **2005**, *43*, 2049–2068. [[CrossRef](#)]
46. Wyllie, P.J.; Tuttle, O.F. The system $CaO-CO_2-H_2O$ and the origin of carbonatites. *J. Petrol.* **1960**, *1*, 1–46. [[CrossRef](#)]
47. Fanelli, M.T.; Cava, N.; Wyllie, P.J. Calcite and Dolomite without Portlandite at a New Eutectic in $CaO-MgO-CO_2-H_2O$ with Applications to Carbonatites. Morphology and Phase Equilibria of Minerals. In *Proceedings of the 13th General Meeting of the International Mineralogical Association, Varna, Bulgaria, 19–25 September 1986*; Bulgarian Academy of Science: Sofia, Bulgaria; pp. 313–322.
48. Drabek, M.; Fryda, J.; Janoushek, V.; Sarbach, M. Regionally Metamorphosed Carbonatite-Like Marbles from the Varied Group, Molanubian Unit, Bohemian Massif, Czech Republic, and their Mo–Th–Nb–REE Mineralization. In *Mineral Deposits: Processes to Processing*; Stanley, C.J., Ed.; Balkema: Rotterdam, The Netherlands, 1999; Volume 1, pp. 635–638.
49. Le Bas, M.J.; Babattat, M.A.O.; Taylor, R.N.; Milton, J.A.; Windley, B.F.; Evins, P.M. The carbonatite–marble dykes of Abyan province, Yemen Republic: The mixing of mantle and crustal carbonate materials revealed by isotope and trace element analysis. *Miner. Petrol.* **2004**, *82*, 105–135. [[CrossRef](#)]
50. Liu, Y.; Berner, Z.; Massonne, H.-J.; Zhong, D. Carbonatite-like dykes from the eastern Himalayan syntaxis: Geochemical, isotopic, and petrogenetic evidence for melting of metasedimentary carbonate rocks within the orogenic crust. *J. Asian Earth Sci.* **2006**, *26*, 105–120. [[CrossRef](#)]
51. Roberts, D.; Zwaan, K.B. Marble dykes emanating from marble layers in an amphibolite-facies, multiply-deformed carbonate succession, Troms, northern Norway. *Geol. Mag.* **2007**, *144*, 883–888. [[CrossRef](#)]
52. Wan, Y.; Liu, D.; Xu, Z.; Dong, C.; Wang, Z.; Zhou, H.; Yang, Z.; Liu, Z.; Wu, J. Paleoproterozoic crustally derived carbonate-rich magmatic rocks from the Daqinshan area, North China Craton: Geological, petrographical, geochronological and geochemical (Hf, Nd, O and C) evidence. *Am. J. Sci.* **2008**, *308*, 351–378. [[CrossRef](#)]
53. Proskurnin, V.F.; Petrov, O.V.; Gavrish, A.V.; Paderin, P.G.; Mozoleva, I.N.; Petrushkov, B.S.; Bagaeva, A.A. The Early Mesozoic carbonatite belt in the Taimyr Peninsula. *Litosfera* **2010**, *3*, 95–102.
54. Schumann, D.; Martin, R.F.; Fuchs, S.; De Fourestier, J. Silicocarbonatitic melt inclusions in fluorapatite from the Yates Prospect, Otter Lake, Quebec: Evidence of marble anataxis in the Central Metasedimentary Belt of the Grenville Province. *Can. Mineral.* **2019**, *57*, 583–604. [[CrossRef](#)]
55. Lentz, D.R. Carbonatite genesis: A reexamination of the role of intrusion-related pneumatolytic skarn processes in limestone melting. *Geology* **1999**, *27*, 335–338. [[CrossRef](#)]
56. Barnes, C.G.; Prestvik, T.; Sundvoll, B.; Surratt, D. Pervasive assimilation of carbonate and silicate rocks in the Hortavaer igneous complex, north-central Norway. *Lithos* **2005**, *80*, 179–199. [[CrossRef](#)]
57. Bowen, N.L. *The Evolution of the Igneous Rocks*; Princeton University Press: Princeton, NJ, USA, 1928; p. 332.
58. Spandler, C.M.; Lukas, H.J.; Pettke, T. Carbonate assimilation during magma evolution at Nisyros (Greece), South Aegean Arc; evidence from clinopyroxene xenoliths. *Lithos* **2012**, *146–147*, 18–33. [[CrossRef](#)]
59. Mollo, S.; Vona, A. The geochemical evolution of clinopyroxene in the Roman Province: A window on decarbonation from wallrocks to magma. *Lithos* **2014**, *192–195*, 1–7. [[CrossRef](#)]